

Evaluation of Scattering in Cone-Beam Breast Computed Tomography: A Monte Carlo and Experimental Phantom Study

Giovanni Mettivier, Paolo Russo, *Member, IEEE*, Nico Lanconelli, and Sergio Lo Meo

Abstract—In this paper Monte Carlo simulations were performed for X-ray irradiations of breast phantoms of various sizes such as PMMA cylinders of different diameters and a hemi-ellipsoidal PMMA phantom. The aim was the evaluation of the 2D distribution of primary and scattered photons and Scatter-to-Primary Ratio (SPR) in projection images in cone-beam breast Computed Tomography (CT). Irradiation geometry and technique factors reproduce the experimental conditions used for validation measurements with a prototype CT breast scanner. Simulations were performed with GEANT4 software. We varied the phantom diameter and shape, the X-ray tube voltage and added filtration. Magnification was 1.31. SPR increases from 0.4 (at 8 cm cylinder diameter) up to 1.5 (14 cm cylinder diameter) at the centre of the phantom. In the same phantom, SPR has lower values toward the bases of the cylinder than at its centre. The scatter component increases by adopting a 50 kVp or higher tube voltages, up to 80 kVp, and by increasing the added filtration. Simulated and measured lateral profiles across a 14 cm cylinder diameter in projection images show a relative deviation of 4%. Simulations show a different distribution of scatter and SPR in a 14 cm diameter cylinder and 14 cm hemi-ellipsoidal phantom, so questioning the use of simple cylindrical geometries when simulating the attenuation of the pendant breast for scatter correction procedures. The strength and the non-uniformity of the SPR inside the cylindrical phantom decrease as the size of the air gap between object and detector increases.

Index Terms—Cone-beam breast computed tomography (CT), Monte Carlo simulations.

I. INTRODUCTION

SEVERAL research groups are working on pendant-geometry Cone-Beam Breast Computed Tomography (CBBCT) as a new methodology in breast tumor diagnosis [1]–[8]. The technique is made possible thanks to improvement in flat panel technology and cone-beam reconstruction algorithms. One of the principal problem in CBBCT, and in general in Cone-Beam

Computed Tomography, is the presence of a great scatter fraction in the projection images as a result of the absence of breast compression and irradiation of the whole organ. This fraction is usually much larger than the one occurring in X-ray mammography with a compressed breast and a low-energy X-ray beam and significant also with respect to fan-beam Computed Tomography (CT), where the cone angle is about ten times lower. The high Scatter-to-Primary Ratio (SPR) reduces the contrast and increases image artifacts and CT number inaccuracy. Therefore, the study and the reduction of this component is an important and actual challenge.

Recently, several studies using both a Monte Carlo (MC) simulation method [9] or empirical techniques [10]–[12] have been reported on the evaluation of the SPR as a parameter to quantify scatter in CBBCT. Techniques for scatter reduction include using air gaps, bow-tie X-ray beam compensator filters [13], antiscatter grids and software correction algorithm or their combination [14].

In this study, MC simulations of PMMA cylinders of different diameters and of a realistic PMMA breast phantom are used to evaluate the 2D scatter distribution in projection images in CBBCT, with a half cone-beam geometry and technique factors that reproduce the experimental setup used for validation measurements. The investigative goal is to analyze the effect of scattered radiation in CBBCT and to optimize the choice of the X-ray beam spectrum.

II. MATERIALS AND METHODS

We simulated PMMA cylinders with different diameters (8, 10, 12, and 14 cm) and 10 cm height and a PMMA breast phantom shaped as a hemi-ellipsoid of semi-axes 7 cm and 9.5 cm, respectively, on a cylindrical base of 14 cm diameter and 3.5 cm height. Simulations were performed in half cone-beam irradiation geometry (Fig. 1) at varying X-ray beam energies (W anode with 80, 70, 60, and 50 kVp) and added filtration (0.1 mm or 0.2 mm Cu) but with the same exposure level of 0.5 μGy air kerma at the isocenter. The average beam energy at 80 kVp was 51.3 keV for 0.2 mm Cu filtration and 48.6 keV for 0.1 mm Cu filtration. The total deposited energy (MeV) at the entrance of the detector was scored in $1 \times 1 \text{ mm}^2$ equivalent pixels over a projection area of $24 \times 24 \text{ cm}^2$. The GEANT4 code system (ver. 4.9.0, with the standard transport model and library of electromagnetic interactions, EMStandard library) was used to model a CBBCT apparatus with a tungsten anode X-ray tube with Cu added filtration and a digital imaging detector. The Standard EM package provides simulation of ionization,

Manuscript received December 22, 2009; revised March 10, 2010; accepted June 04, 2010. Date of publication August 23, 2010; date of current version October 15, 2010.

G. Mettivier and P. Russo are with the Dipartimento di Scienze Fisiche, Laboratory of Medical Physics, Università di Napoli Federico II, I-80126 Napoli, Italy and also with INFN, Sezione di Napoli, I-80126 Napoli, Italy (e-mail: mettivier@na.infn.it).

N. Lanconelli and S. L. Meo are with the Dipartimento di Fisica, Alma Mater Studiorum—Università di Bologna, I-40126 Bologna, Italy and also with INFN, Sezione di Bologna, I-40126 Bologna, Italy.

Color versions of one or more of the figures in this paper are available online at <http://ieeexplore.ieee.org>.

Digital Object Identifier 10.1109/TNS.2010.2053050

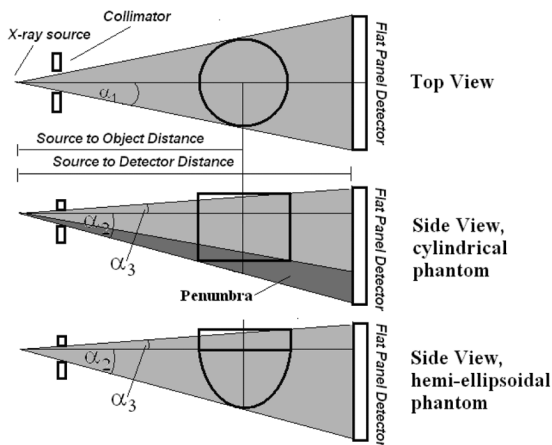


Fig. 1. Top and lateral view of the half cone-beam geometry, where α_1 and $(\alpha_2 + \alpha_3)$ are the fan angle and cone angle, respectively. A cylindrical phantom and a hemi-ellipsoidal phantom, both of PMMA and 14 cm diameter at their base, have been imaged. The effect of the presence of a “penumbra” by cone-beam irradiation of the cylindrical phantoms is illustrated in the text.

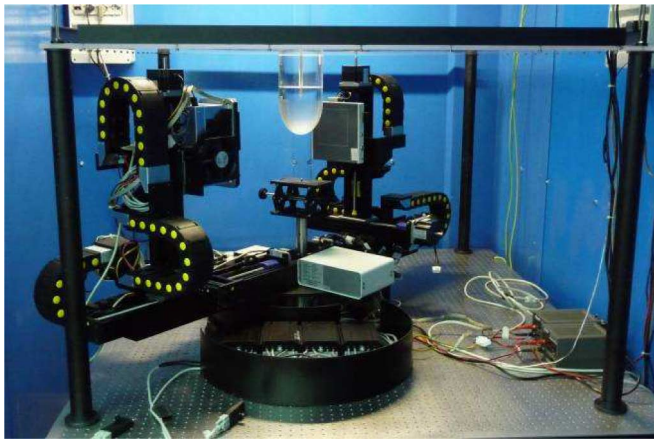


Fig. 2. Bench-top prototype for Cone-Beam Breast Computed Tomography developed at the University and INFN of Naples, Italy. A hemi-ellipsoidal PMMA phantom is visible at the scanner isocenter, to simulate a pendant breast.

bremsstrahlung and other Electro-Magnetic interactions of particles with matter. More details about the physics implemented in the EMStandard library and its application can be found in [15]–[17].

For the W anode X-ray tube, simulated spectra from Boone’s TASMIP MC code [18] were used for the 50–80 kVp beams with 1% ripple. We tallied the photons impinging on the detector area, separating results for primary photons and photons having undergone scattering within the phantom. For each pixel the SPR was estimated as the ratio between the energy deposited by scattered and primary photons.

The MC model was validated with a bench-top apparatus for X-ray CBBCT (Fig. 2), assembled at the University and INFN in Napoli for evaluation and for laboratory tests of various optimization techniques for CBBCT [8].

The prototype is characterized by the computer-control of the X-ray tube (W anode, 35–80 kVp tube voltage range, 0.02–0.25 mA tube current range, continuous output, 1.8 mm Al intrinsic filtration and Cu added filtration), CsI:TI CMOS flat panel detector (Hamamatsu C7942CA-02, $12 \times 12 \text{ cm}^2$ area, $50 \mu\text{m}$

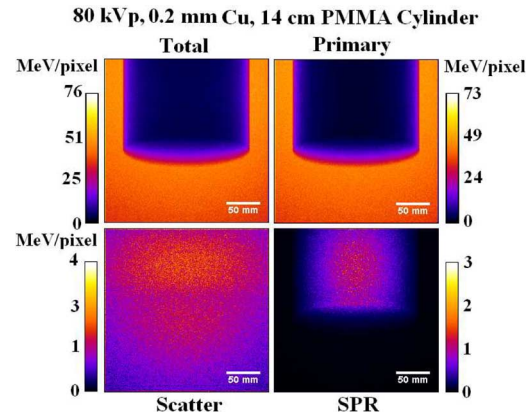


Fig. 3. Monte Carlo simulated projection images (total, primary, scatter components) and Scatter-to-Primary Ratio (SPR) 2D distribution of 14 cm diameter PMMA cylinder at 80 kVp and 0.2 mm Cu added filtration, $\text{HVL} = 5.6 \text{ mm Al}$. The number of photon histories in the simulation was determined so as to correspond to an air dose of $0.5 \mu\text{Gy}$ at the scanner isocenter, where the axis of the cylinder was positioned.

pitch, frame rate up to 9 fps at 4×4 binning), step-motor translation and rotation stages with eight degrees of freedom, fan-beam or cone-beam back-projection software [8]. The scanner works in step-and-shoot as well as in continuous acquisition mode. All images were processed with the ImageJ public-domain software (<http://rsbweb.nih.gov/ij/>).

CT scans of a homogeneous PMMA cylinder (14 cm diameter, 10 cm height) and of the previously described PMMA hemi-ellipsoidal phantom were performed with the described prototype. Experimental results of this set-up (which simulates the scan of an uncompressed pendant breast) were compared with MC simulations. Measurements were performed with the half cone-beam irradiation geometry, at a fixed tube voltage of 80 kVp and with a tube current of 0.25 mA. Phantoms were placed at the scanner isocenter at a source-to-detector distance of 50.5 cm and a source-to-object distance of 38.5 cm. System magnification was 1.31 at the isocenter. To acquire projections with the same Field of View (FoV) ($24 \times 24 \text{ cm}^2$) as in simulated projections, with the limited area ($12 \times 12 \text{ cm}^2$) X-ray detector, successive horizontal and vertical translations of the detector were made in the image plane, in a 2×2 mosaic. The acquisition time per single frame was 60 s and 240 s for a full projection ($24 \times 24 \text{ cm}^2$). Projections were corrected for offset and gain (flat-field).

Given the tube voltage (80 kVp) and 0.2 mm Cu added filtration, the tube current (0.25 mA), the tube load (15 mAs), for each projection we measured a free-air-kerma of $7 \mu\text{Gy}$ at the scanner isocenter. Exposure measurements were performed with a calibrated ionization chamber (in-beam ion chamber model no. 20X6-6, Radcal Corporation, Monrovia, CA, USA, sensitive volume 6 cm^3 , readout by a Radcal mod. 2026C dosimeter). In order to compare measurements with simulations, the projections were off-line further binned 5×5 to obtain the dimensions ($1 \times 1 \text{ mm}^2$) of simulated pixel. With this ion chamber, Half Value Layer (HVL) measurements were performed at 80 kVp in good geometry and 99.999% pure Al filters (0.2 mm Cu added filtration), giving $\text{HVL} = 5.6 \text{ mm Al}$.

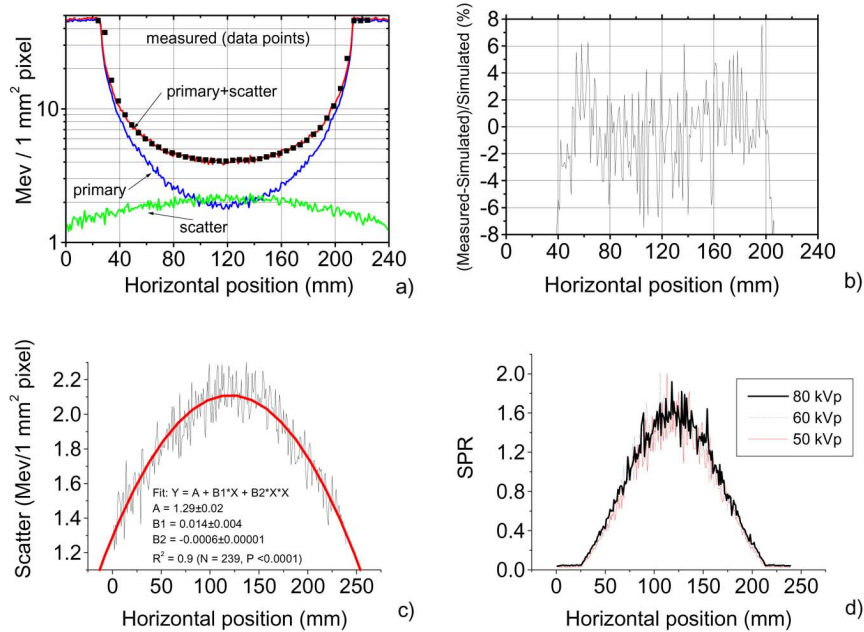


Fig. 4. (a) Simulated and measured profiles along the horizontal axis of a 14 cm diameter PMMA cylinder at 80 kVp, 0.2 mm Cu filter, air kerma at isocenter = $0.5 \mu\text{Gy}$ for simulations, $7 \mu\text{Gy}$ for measurements. (b) Normalized difference between measured and simulated profiles of data in a) for total (primary + scatter) projection images, showing a relative variation of 4% (std. dev.). Magnification is 1.31. (c) For the scatter fraction data in a) a parabolic fit through the simulation data has been performed (bold line), which allows to estimate accurately the scatter contribution both inside and outside the phantom. (d) SPR horizontal distribution at 80, 60 and 50 kVp, at the center of the cylindrical phantom. The three distributions are almost overlapping.

TABLE I
FITTED GAUSSIAN PARAMETERS $y = A \exp[-0.5(X/\sigma)^2]$ FOR THE 14 CM
DIAMETER PMMA PHANTOM

kVp	A	σ (mm)	χ^2
50	1.58	50.0	0.012
60	1.61	50.4	0.010
80	1.65	51.4	0.008

III. RESULTS

A. Model Validation

The MC validation was obtained through the comparison between simulated and measured projections of the same phantom. An example set of the simulation results with a 14 cm diameter PMMA cylinder at 80 kVp is shown in Figs. 3–5. Fig. 3 shows the simulated primary, scatter and primary plus scatter (total) components in projection images at 80 kVp and 0.2 mm Cu added filtration, for a PMMA cylinder of 14 cm diameter. The SPR 2D distribution is also shown in Fig. 3. Profiles across a cylinder diameter, in simulated and measured projection at 80 kVp, are reported in Fig. 4(a) after scaling the data for the different exposures. In Fig. 4(b), a comparison between simulated and measured line profiles (primary + scatter) is proposed. Fig. 4(c) analyzes the shape of the scatter horizontal distribution and Fig. 4(d) shows the horizontal profile of the SPR at 80, 60 and 50 kVp. These profiles have the shape of a Gaussian distribution, in agreement with the finding reported in [12]. We fitted these three curves to a Gaussian function: $y = A \exp[-0.5(x/\sigma)^2]$, and the resulting parameters are listed in Table I.

PMMA 14 cm diameter 80 kVp 0.2 mm Cu

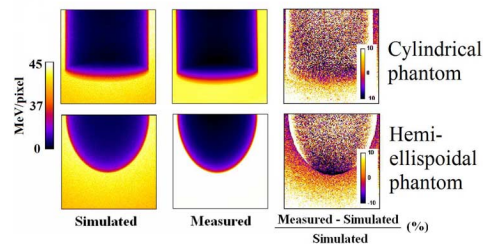


Fig. 5. Simulated (primary + scatter), measured and relative difference between measured and simulated projections of a 14 cm diameter PMMA cylinder and a 14 cm hemi-ellipsoidal phantom simulating the pendant breast irradiated at 80 kVp, and 0.2 mm Cu added filtration ($\text{HVL} = 5.6 \text{ mm Al}$) using the prototype CBBCT scanner. In MC simulations deposited energy is scored in $1 \times 1 \text{ mm}^2$ pixels.

We observe that the scale factor k introduced for data registration between pixel values (ADU) in acquired images and pixel values (MeV) in simulated images is $k = 22 \text{ ADU/MeV}$, which takes into account both the flat panel detection efficiency and the different exposure levels between simulation and experiment.

Fig. 5 shows the direct comparison between simulated and acquired images with the CBBCT projections of both phantoms (14 cm diameter cylinder and 14 cm diameter hemi-ellipsoidal PMMA phantom). The phantoms were imaged at 80 kVp with 0.2 mm Cu added filtration. The corresponding horizontal and vertical line profiles (defined as in Fig. 6(c)) are shown in Fig. 6(a) and in Fig. 6(b) for the case of the hemi-ellipsoidal phantom. The vertical profile is through the central axis of the phantom from the top (“chest wall”) to the bottom (“nipple”).

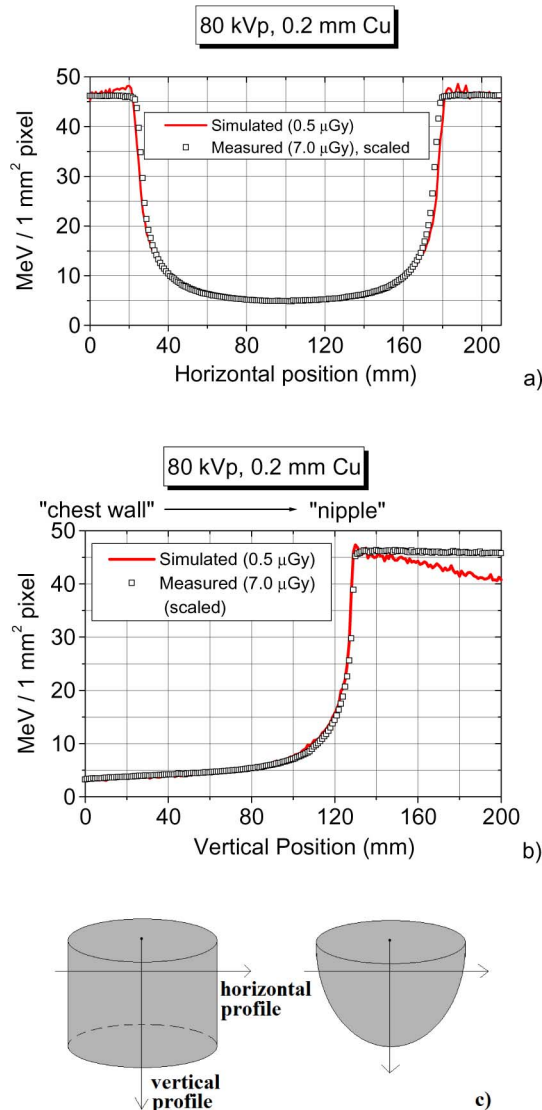


Fig. 6. Simulated and measured profiles along the (a) horizontal (at a distance of 5 cm from the top base) and (b) vertical central axis of 14 cm diameter PMMA hemi-ellipsoidal phantom at 80 kVp, 0.2 mm Cu filtration, air kerma at isocenter = 0.5 μ Gy for simulations, 7 μ Gy for measurements. (c) Geometry for evaluating the profiles in the phantoms.

B. Scatter Evaluation

Fig. 7 reports the simulated 2D scatter distributions obtained by varying the X-ray beam energy (80, 70, 60, and 50 kVp), beam filtration (0.1 mm or 0.2 mm Cu) and PMMA cylinder diameter (8, 10, 12, 14 cm).

Fig. 8 shows the profiles of the simulated scatter values at 50 kVp (0.1 mm Cu added filtration) along the vertical axis of the four cylinders (with diameter 8, 10, 12 or 14 cm, respectively). These profiles are estimated from the images shown in the upper row in Fig. 7 (the four images on the left). In Fig. 9, an evaluation of the scatter component within the phantom is presented, for all the simulated X-ray beams and all the phantom diameters.

C. SPR Evaluation

In Fig. 10, an example of 24×24 cm² 2D distribution of SPR is shown, for the case of the 8 cm diameter PMMA cylinder.

By selecting three different ROIs (A, B, C) in this distribution as indicated in Fig. 10, it is possible to study the variation of the mean value inside the ROI as a function of the cylinder diameter, at various kVp and Cu filter thicknesses. The 30×30 mm² ROIs A, B, C are positioned on the central axis of the PMMA cylinder, at 20, 60 and 100 mm from the top surface (“chest wall”), respectively. The results are reported in Fig. 11(a). SPR increases from $\cong 0.4$ (at 8 cm cylinder diameter) up to 1.5 (14 cm cylinder diameter) at the center of the phantom. SPR (ROIs A and C) has lower values toward the bases of the cylinder than at its center (ROI B). The SPR data for the innermost ROI (B) were well fitted by a quadratic function as a function of the cylinder diameter (Fig. 11(b)).

In the case of the hemi-ellipsoidal phantom, the SPR distribution at 80 kVp, 0.2 mm Cu, is shown in Fig. 12(b), in comparison with the analogous distribution for a PMMA cylinder of 14 cm diameter (Fig. 12(a)).

D. Scatter Distribution

The 2D distributions of the scatter component due to the different shape of the phantom (cylinder or hemi-ellipsoid) were also evaluated. In Fig. 13, are shown a planar and surface rendering visualization of simulated 2D scatter distribution of 14 cm diameter cylinder and 14 cm diameter hemi-ellipsoidal phantom.

E. Influence of the Air Gap

In all simulations shown previously, the object-to-detector distance was fixed at 12 cm (magnification = 1.31), which for a 14 cm diameter phantom placed at the isocenter implies an air gap of just 5 cm. An increase of the air gap is expected to be effective in reducing the SPR, in particular on-axis [12], [19]. In order to investigate the effect of the air gap, we made another simulation (with source-to-object distance of 40 cm); in Fig. 14(a) is shown the vertical profile of the SPR (from chest wall to nipple) as a function of the distance from the axis of the object (isocenter) to the detector, at 80 kVp for a PMMA cylinder of 14 cm diameter. The range of distances selected (10–25 cm) corresponds to air gaps of 3–18 cm between the phantom and the detector. The corresponding vertical profiles for the scatter component are shown in Fig. 14(b).

IV. DISCUSSION

The relative deviation between the primary + scatter and measured profiles reported in Fig. 4(a), is comprised in a range of $\pm 4\%$ (std. dev.) giving indication of a reasonable agreement between simulated and acquired data. Moreover, from Fig. 4(a) it is possible to note that the scatter component—determined over a total span of 24 cm in the image plane across the 14 cm wide phantom—increases toward the central axis of the phantom and its profile has a parabolic shape (Fig. 4(c)), in agreement with other studies [11]. A simulated scatter component decreasing from the center toward the edges of the cylindrical phantom has also been reported in [19] at 50 kVp for a cylindrical breast phantom, at variance with another report [12] which found decreasing scatter toward the center of a cylindrical breast phantom of 14 cm diameter.

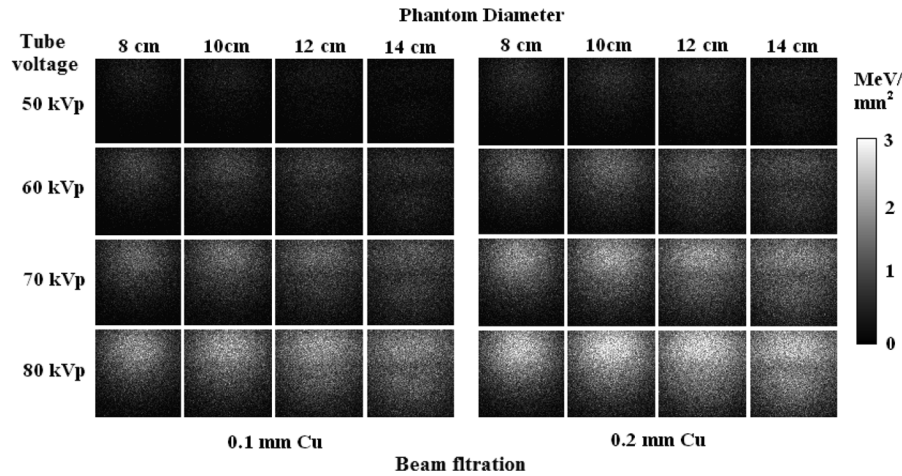


Fig. 7. Simulated 2D scatter distributions in 8–14 cm diameter PMMA cylinders as a function of X-ray tube voltage and added Cu filtration. Exposure level is fixed at $0.5 \mu\text{Gy}$ air kerma at isocenter. Rows refer to varying tube voltages and columns refer to varying phantom diameters.

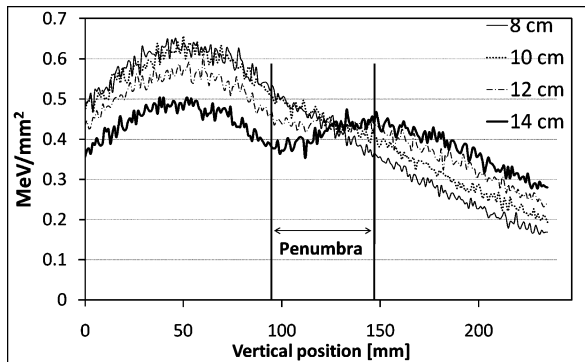


Fig. 8. Profiles along the vertical axis of the image of the scatter component simulated for the four diameters PMMA cylinder at 50 kVp and 0.1 mm Cu added filtration (pictures of the upper row in Fig. 7). The 14 cm diameter plot shows an increase of the scatter due to the penumbra of the cylinder.

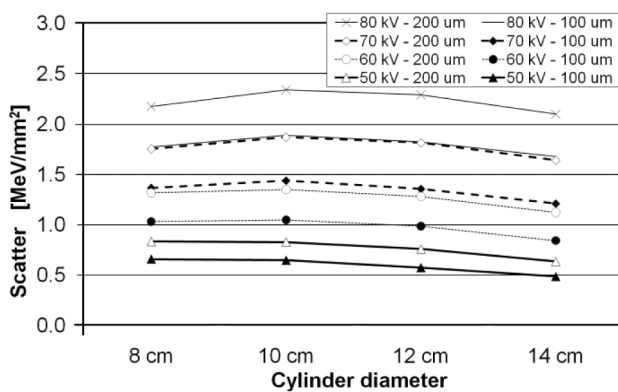


Fig. 9. Scatter component evaluated on ROI B (see Fig. 10) for all the simulated X-ray beams as a function of the phantom diameter. Here, cylindrical PMMA phantoms are considered for all the simulations.

The SPR horizontal distribution across the cylindrical PMMA phantom (Fig. 4(d)) decreases toward the edges of the cylindrical phantom, as reported in [18] at 50 kVp and at (40, 60, 80, 100 kVp) in [12], for breast tissue phantoms. Fig. 4(d) also indicates that the SPR distribution is independent of the tube voltage from 80 kVp to 60 kVp, in agreement with reports in [12].

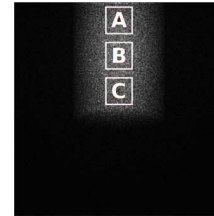


Fig. 10. Example of a 2D simulated SPR distribution over a $24 \times 24 \text{ cm}^2$ FOV (for the 8 cm diameter cylindrical PMMA phantom irradiated with the 50 kVp, 0.2 mm Cu filter beam). Three ROIs are indicated (A, B, C) for quantitative evaluations. Each ROI covers an area of $30 \text{ mm} \times 30 \text{ mm}$ and is located on the central axis of the phantom. The centers of ROIs A, B, and C are located at a distance of 20 mm, 60 mm, and 100 mm from the chest wall, respectively.

We note that the SPR values in the present work ($\text{SPR} \cong 1.5$ on-axis, 80 kVp, 14 cm diameter PMMA cylinder) are much higher than those reported for breast tissue phantoms of the same shape and size ($\text{SPR} = 0.46$ on-axis, 80 kVp, 14 cm diameter cylinder [12]; $\text{SPR} = 0.56$ on-axis, 50 kVp, 14 cm diameter cylinder [18]). This might result from the differences in the material and in the irradiation geometry (fan and cone angle, and particularly, the presence of a larger air gap), with major influence of the phantom-to-detector distance. For example, reducing the air gap increases the SPR quadratically [18] and extrapolating the data in [18] to the short air gap in the present work (12 cm isocenter to detector axis, $\text{airgap} = 5 \text{ cm}$), we estimate $\text{SPR} \cong 1.3$ on-axis for a breast tissue phantom. Analogous considerations apply with reference to simulations in [12], where the air gap was 24.5 cm. To illustrate further this point, Fig. 14(a) indicates a reduction by a factor 2.5 of the maximum SPR on increasing the object-to-detector distance from 10 cm ($\text{SPR} \cong 1.3$) to 25 cm ($\text{SPR} \cong 0.5$). Moreover, the SPR flattens inside the phantom at increasing object-to-detector distance, due to the reduction of the scatter component in projection images at increasing air gap (Fig. 14(b)). At short object-to-detector distances, significant cupping artifacts due to scattering are predicted in CT scans (and indeed observed [8]) from this trend: distances of 20–25 cm are effective in reducing the SPR

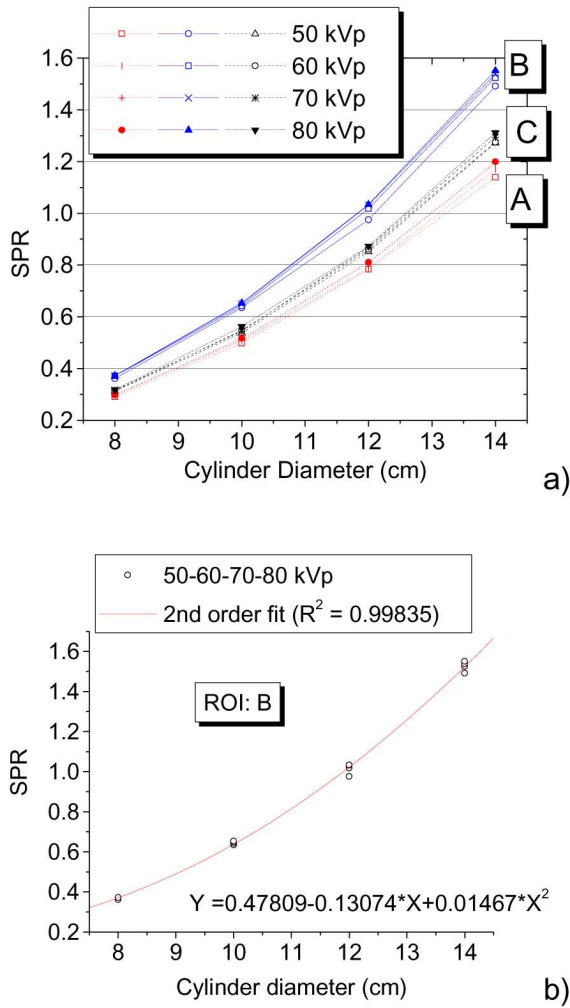


Fig. 11. (a) Simulated SPR mean values, inside the ROIs A, B and C as indicated in Fig. 10, as a function of the cylinder diameter of PMMA phantoms, at different X-ray tube voltages (50, 60, 70, 80 kVp) and 0.2 mm Cu added filtration. (b) The data for ROI B at all voltages have been fitted with a second order polynomial.

significantly (e.g., in the case of the Albion scanner at UC Davis, the isocenter-to-detector distance is 31.5 cm [12]).

Simulations and measurements for a cylindrical and a hemi-ellipsoidal phantom have been compared in Figs. 5 and 6 (80 kVp, 0.2 mm Cu), respectively, for the primary plus scatter fields. A close agreement between the two datasets has been observed: relative differences of 1.7% and 3% with respect to simulations were measured for the 86 mm wide central part of the cylindrical and hemi-ellipsoidal phantom, respectively. The discrepancy between measurements and simulations visible outside the phantom in Fig. 6 are due to the fact that the measurements originate from flat-field corrected images, at variance with simulations.

From the qualitative analysis of the image data shown in Fig. 7, the scatter component is higher at 80 kVp than at 50 kVp and it is higher with 0.2 mm than with 0.1 mm added Cu filtration. From the profiles reported in Fig. 8, it is possible to note the presence of a maximum intensity of scattered energy at the centre of phantom (i.e., at 50 mm height from the cylinder base, or “chest wall”). Moreover, for the 14 cm

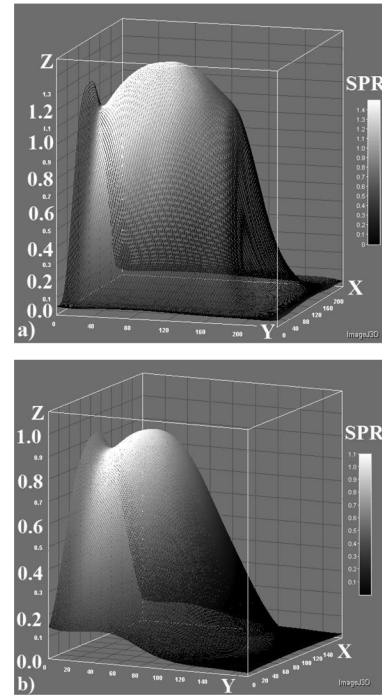


Fig. 12. Comparison of the 2D SPR distribution (surface rendering plots) inside a PMMA phantom of 14 cm diameter and a cylindrical (a) or a hemi-ellipsoidal (b) shape, in projections at 80 kVp and 0.2 mm Cu filtration. In both plots, the phantom base (“chest wall”) is located at $Y = 0$.

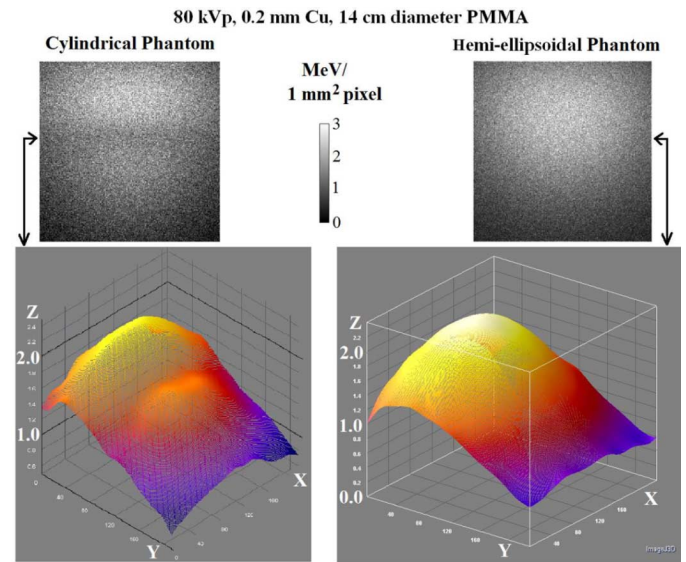


Fig. 13. Comparison in planar (top images) and surface rendering mode (bottom images) between the simulated 2D scatter distributions of a 14 cm diameter PMMA cylinder and a 14 cm diameter base hemi-ellipsoidal phantom simulating the pendant breast. The phantom base (“chest wall”) is located at $Y = 0$.

phantom diameter the scatter component outside the phantom (vertical distance greater than $\cong 150$ mm from the chest wall) is almost comparable with that behind the phantom. This effect is in some way related to the presence of a “penumbra” effect due to the reduction of traversed PMMA thickness (Fig. 1). In Fig. 7, it is indeed more clearly visible for the

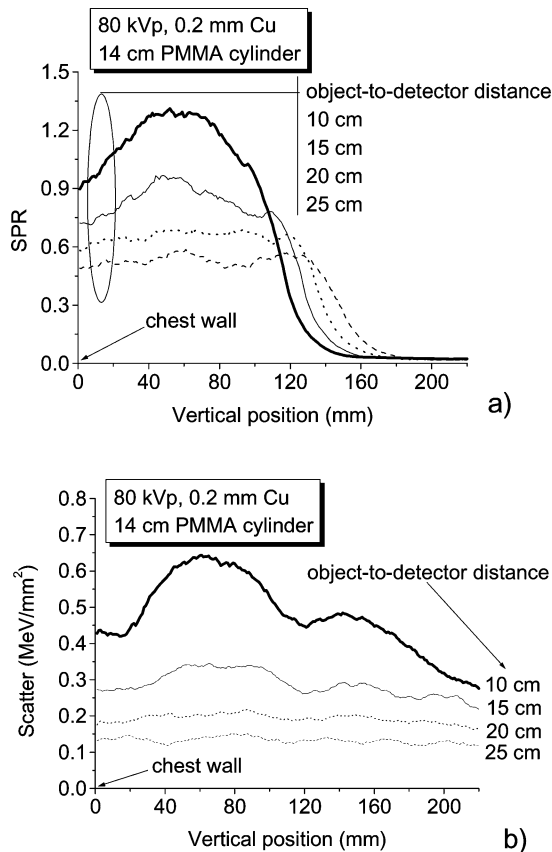


Fig. 14. Smoothed vertical profiles (from the “chest wall” to the “nipple” along the axis of the phantom) of (a) SPR and (b) scatter component, simulated for a PMMA cylinder of 14 cm diameter (80 kVp, 0.2 mm Cu). The curves are relative to varying distances of the phantom axis (isocenter) to the detector plane (10, 15, 20 and 25 cm, respectively). For this simulation, the source-to-object distance was 40 cm.

thickest phantom (14 cm diameter) and for the less energetic X-ray beam (50 kVp with 0.1 mm Cu filter).

In Fig. 9, as already noticed, it is confirmed that the more energetic spectra provide a larger scatter component, with respect to the 50 kVp X-ray beams.

From the analysis of Figs. 7 and 8 we also note that increasing the diameter of the phantom does not always increase the amount of scatter produced. Indeed, if we increase the diameter of the phantom, first the scatter component increases, then a maximum can be reached (in our case at about 10 cm diameter), and finally for the thickest phantoms the scatter component decreases (probably because of self-absorption of the scattered radiation within the phantom). A similar trend was also observed by other researchers [9].

The results reported in Fig. 11(a) indicate that the SPR depends on the cylinder diameter and on the axial position in the phantom, rather than on X-ray tube kilovoltage. From Fig. 11(a), we note that SPR increases from $\cong 0.3$ – 0.4 (at 8 cm cylinder diameter) up to 1.5 (14 cm cylinder diameter) at the centre of the phantom. Fig. 11(b) illustrates the quadratic increase of SPR vs. diameter, D , of the phantom ($\text{SPR} = 0.478 - 0.131 \cdot D + 0.015 \cdot D^2$). SPR (ROIs A and C in Fig. 10) has lower values toward the two bases of the cylinder than at its centre (ROI B). It is worth noting that the choice of the X-ray tube kilovoltage

has a minimal impact on the estimated SPR in the energy range here investigated (50–80 kVp), as already pointed out by other authors [12].

As regards the phantom geometry, Fig. 12 shows a different distribution of the SPR in a PMMA cylinder and in a PMMA hemi-ellipsoidal phantom, at 80 kVp. In this last case, the maximum of the SPR occurs closer to the “chest wall” (at a distance of about 50 mm) than in the case of the cylindrical phantom (distance of about 60 mm). Moreover, for the hemi-ellipsoidal geometry the SPR is a rapidly decreasing function of the vertical position in going from the maximum to the “nipple”; its maximum value ($\text{SPR} \cong 1.0$) is lower than the corresponding maximum value for a cylindrical phantom of the same diameter ($\text{SPR} \cong 1.35$).

From Fig. 13, it is possible to note the presence of two peaks in the distribution of the scatter component inside the cylindrical phantom with respect to the single peak of the scatter distribution inside the hemi-ellipsoidal phantom of the same diameter at its base. This feature is due to the “penumbra” effect described previously. Hence, the different geometry of the phantoms determines a different internal distribution of scatter. For the cylindrical phantom, this effect is more pronounced for short object-to-detector distances (Fig. 14(b)).

V. CONCLUSIONS

Using Monte-Carlo methods we have estimated primary, scatter and scatter-to-primary ratio distributions in 8–14 cm diameter PMMA cylinders and in a 14 cm diameter hemi-ellipsoidal phantom, simulating the average pendant breast, as a function of X-ray tube voltage and added filtration.

Though an ellipsoidal shape is a better representation of a pendant breast geometry, a cylindrical phantom was simulated more extensively in this work, this being the most studied geometry [12], [19]. The SPR increases from 0.4 (at 8 cm cylinder diameter) up to 1.5 (14 cm cylinder diameter) at the centre of the phantom. SPR has lower values at the upper base (0.3–1.2) and at the lower base (0.3–1.3) of the cylinder, than at its centre. While the scatter fraction increases from 50 kVp to 80 kVp and by increasing the added filtration, the SPR does not depend on the beam quality. Then, the choice of the best beam spectrum relies on other parameters (i.e., image quality and patient dose). The MC investigation of the absorbed dose in a PMMA phantom as a function of the beam quality will be the subject of a future work of our group. The simulation data for 80 kVp, 14 cm diameter cylinder, differ from the measured data by less than 4%. Simulations show that the SPR strength and distribution inside a cylindrical phantom depend on the extent of the air gap, with less intense and more uniform SPR for higher air gaps. Simulations also show a different distribution of scatter and of SPR in a 14 cm diameter cylinder and 14 cm hemi-ellipsoidal phantom. This indicates that it may not be correct to make imaging scatter corrections using a cylindrical phantom shape as a realistic breast phantom.

REFERENCES

- [1] J. M. Boone *et al.*, “Dedicated breast CT: Radiation dose and image quality evaluation,” *Radiology*, vol. 221, pp. 657–667, 2001.

- [2] S. J. Glick, "Breast CT," *Annu. Rev. Biomed. Eng.*, vol. 9, pp. 501–526, 2007.
- [3] J. M. Boone *et al.*, "Technique factors and their relationship to radiation dose in pendant geometry breast CT," *Med. Phys.*, vol. 32, pp. 3767–3776, 2005.
- [4] B. Chen and R. Ning, "Cone-beam volume CT breast imaging: Feasibility study," *Med. Phys.*, vol. 29, pp. 755–770, 2002.
- [5] M. P. Tornai *et al.*, "Design and development of a fully 3D dedicated x-ray computer mammotomography system," *Proc. SPIE*, vol. 5745, pp. 189–197, 2005.
- [6] W. T. Yang *et al.*, "Dedicated cone-beam breast CT: Feasibility study with surgical mastectomy specimen," *Amer. J. Roengenol.*, vol. 189, pp. 1312–1315, 2007.
- [7] Dedicated CT of the Female Breast: Feasibility, Optimisation and Comparison to Competing Imaging Modalities, Seventh Research Framework Programme—Euratom [Online]. Available: <http://www.imp.uni-erlangen.de/BreastCT>
- [8] P. Russo *et al.*, "X-ray cone-beam breast computed tomography: Phantom studies," *IEEE Trans. Nucl. Sci.*, vol. 57, no. 1, pp. 160–172, Feb. 2010.
- [9] G. Jarry *et al.*, "Characterization of scattered radiation in kV CBCT images using Monte carlo simulations," *Med. Phys.*, vol. 33, pp. 4320–4329, 2006.
- [10] J. H. Siewerdsen and D. A. Jaffray, "Cone-beam computed tomography with a flat-panel imager: Magnitude and effects of x-ray scatter," *Med. Phys.*, vol. 28, pp. 220–231, 2001.
- [11] J. H. Siewerdsen *et al.*, "A simple, direct method for x-ray scatter estimation and correction in digital radiography and cone-beam CT," *Med. Phys.*, vol. 33, pp. 187–197, 2006.
- [12] A. L. C. Kwan, J. M. Boone, and N. Shah, "Evaluation of x-ray scatter properties in a dedicated cone-beam breast CT scanner," *Med. Phys.*, vol. 32, pp. 2967–2975, 2005.
- [13] S. A. Graham *et al.*, "Compensators for dose and scatter management in cone-beam computed tomography," *Med. Phys.*, vol. 34, pp. 2691–2703, 2007.
- [14] R. Ning and X. Tang, "X-ray scatter correction algorithm for cone beam CT imaging," *Med. Phys.*, vol. 31, pp. 1195–1202, 2004.
- [15] S. Agostinelli *et al.*, "GEANT4 a simulation toolkit," *Nucl. Instrum. Methods Phys. Res. A*, vol. 506, pp. 250–303, 2003.
- [16] J. Allison *et al.*, "Geant4 developments and applications," *IEEE Trans. Nucl. Sci.*, vol. 53, no. 1, pp. 270–278, Feb. 2006.
- [17] K. Amako *et al.*, "Comparison of Geant4 electromagnetic physics models against the NIST reference data," *IEEE Trans. Nucl. Sci.*, vol. 52, no. 4, pp. 910–918, Aug. 2005.
- [18] J. M. Boone and J. A. Seibert, "An accurate method for computer-generating tungsten anode x-ray spectra from 30 to 140 kV," *Med. Phys.*, vol. 24, pp. 1661–1670, 1997.
- [19] Y. Chen *et al.*, "Characterization of scatter in cone-beam CT breast imaging: Comparison of experimental measurements and Monte Carlo simulation," *Med. Phys.*, vol. 36, pp. 857–869, 2009.